

Experimental investigation of the interaction of a weak planar shock with grid turbulence in a counter-driver shock tube

Takahiro Tamba,^{*} Gaku Fukushima, Masaya Kayumi,[†] Akira Iwakawa, and Akihiro Sasoh[‡]
Department of Aerospace Engineering, Nagoya University, Nagoya 464-8603, Japan



(Received 30 May 2018; published 26 July 2019)

The impacts of the interaction with grid turbulence of a turbulent Mach number in the range 0.6×10^{-2} to 2.4×10^{-2} (representative value) on a planar shock wave with a shock Mach number of about 1.04 were experimentally investigated. Using the counter-driver shock tube with a 120 mm \times 120 mm square cross section, the turbulent Mach number level and the interaction length at the observation section were varied independently. Within resolvable experimental data, the shock Mach number became a decreasing function of the interaction length. The thickness of the shock front side-view profile increased as the turbulent Mach number and the interaction length increased. With a turbulent Mach number of 2.4×10^{-2} (representative value) and an interaction length longer than 200 mm, the shock front profile became fragmented. The condition for the fragmentation is consistent with the “broken shock” criterion proposed by numerical studies.

DOI: [10.1103/PhysRevFluids.4.073401](https://doi.org/10.1103/PhysRevFluids.4.073401)

I. INTRODUCTION

Shock wave–turbulence interaction involves the stochastic modulation of pressure appearing, for example, in sonic boom behavior past atmospheric turbulence [1,2]; in some cases the peak value in the post-shock pressure is enhanced, and in other cases it is weakened and the pressure rise time is increased. The elementary processes of the interaction between a shock wave and counterflow are well explained by Ribner *et al.* [3]: if the counterflow is toward the shock wave, the shock Mach number, which is defined as the ratio of the shock wave propagation speed relative to the gas in front of it to the speed of sound, is increased so that the post-shock pressure is increased and the shock wave front is deformed in a concave shape toward the propagation direction; if the counterflow is in the same direction as the shock wave propagation, the shock Mach number is decreased, the post-shock pressure is also decreased, and the shock wave front becomes convex. In a whole shock wave–turbulence interaction field, such elementary processes under various conditions appear in a spatiotemporally random manner; the overall impact on the pressure field needs to be quantified in a systematic manner.

In order to simply characterize the problem, the combination of a plane shock wave and canonical turbulence is a good starting point. However, in experiments it is difficult to realize them simultaneously. A blast wave is generated by a point source or its equivalent, for example, electrical discharge [4], laser-induced breakdown [5], explosive [6], and even from an open end of a shock tube [7–9]. However, in such cases, due to expansion waves the post-shock overpressure rapidly

^{*}Present address: National Institute of Advanced Industrial Science and Technology (AIST), Central 5, 1-1-1, Higashi, Tsukuba, Ibaraki 305-8565, Japan.

[†]Present address: Mitsubishi Heavy Industries, Ltd., Turbomachinery No. 2 Laboratory Fluid Dynamics Research Department Research & Innovation Center, 2-1-1 Shinhamma Arai-cho, Takasago 676-8686, Japan.

[‡]Corresponding author: akihiro.sasoh@mae.nagoya-u.ac.jp

decreases with the distance from the wave front; it is difficult to investigate the effect of propagation length on the pressure modulation.

The method of generating turbulence is also limited in many shock wave generation systems. Barre *et al.* [10,11] experimentally investigated the impacts of a normal shock wave on quasi-homogeneous turbulent flow in a Mach 3 wind tunnel. The normal shock wave was generated as a Mach stem in the reflection between two oblique shock waves over symmetrically set wedges. The turbulent flow was generated by using an array of small nozzles set upstream from the shock wave. It was confirmed that small-scale turbulent spectra were more amplified. However, due to the difficulty in characterizing the turbulence, obtained insights were quite limited. Lipkens and Blackstock [4] used a slit jet to interact with a blast-like shock wave. When passing through the jet, the pressure rise time is mostly increased. The ensemble average of the peak pressure is slightly decreased, yet the standard deviation of the peak pressure is much larger than the decrease in the ensemble average. Kim *et al.* [5] visualized similar shock wave interaction using a Schlieren setup. Such an approach worked well to experimentally demonstrate the impact of turbulent flow on the post-shock pressure moderation. However, it is difficult to quantitatively relate the modulation characteristics to the turbulence characteristics.

In principle, by using a shock tube it is possible to generate both grid turbulence behind a shock wave and a plane shock wave propagating in the opposite direction to interact with each other. Using a shock tube, Dosanjh [12] generated turbulent flow behind the shock wave past grids. Moreover, after the shock wave was reflected from the end wall, the reflected shock wave interacted with the post-incident-shock grid turbulence and its wave front became perturbed. Honkan *et al.* [13,14], Xanthos *et al.* [15], and Agui *et al.* [16] employed and extended this methodology by making the incident shock wave reflect from a porous wall so that the strength of the reflected shock wave could be weakened, yet in principle not be strengthened. Without the porous wall, the characteristics of the reflected shock wave were uniquely related to those of the incident shock wave. Even by using porous walls, the characteristics of the reflected shock wave could not be widely varied because the porosity and thickness of the porous wall could be varied only in a discrete manner. Moreover, the interaction length observable at the test section could not be controlled independently.

So far, important insights on the shock wave–turbulence interaction have been obtained mostly from numerical investigations, most of which emphasize the effects of shock wave compression on the variation of turbulence parameters [17–23]. Lee *et al.* [17] and Larsson *et al.* [18,24] numerically investigated the interaction between canonical turbulence and a normal shock wave at different shock Mach numbers, M_s , turbulent Mach numbers, M_t , and Reynolds numbers. The jumps in mean density and pressure across the shock wave became lower as compared with those of non-turbulent Rankine-Hugoniot results by a factor of M_t^2 [24], which is qualitatively consistent with Lele’s theory [25]. In particular, the authors highlighted the appearance of “broken shock” past which the flow variables do not experience a jump, and suggested some criteria for the appearance of broken shock as $M_t^2 \geq 0.1(M_s^2 - 1)$ [17], $M_t^2 \geq 0.06(M_s^2 - 1)$ [18], and $M_t \geq 0.6(M_s - 1)$ [19,20,24]. However, in those numerical works, since the primary interest is the effect on the turbulence the shock Mach number is set constant by manipulating the boundary condition on the driving side of the shock wave. However, such a situation is different from the above-mentioned practical one like a sonic boom past atmospheric turbulence. In order to reproduce phenomena observed in many practical cases, the “shock tube condition” in which the shock wave is driven by a driver section at a given initial pressure should be employed. In that case, the shock wave becomes modulated according to the propagation length through the turbulence zone.

Tamba *et al.* [26] improved the function of the shock tube by developing a “counter-driver shock tube” (CD-ST), which is a shock tube having two high-pressure channels as independent drivers on both sides of a low-pressure channel so that the interaction between a shock wave and a counterflow can be investigated experimentally. The operation conditions of each driver are set independently so that the conditions of the shock wave and those of the counterflow can be set independently. Moreover, by varying the mutual driver operation timings, the interaction length observable in the test section can be varied. In this study, using a newly developed CD-ST with larger dimensions, we

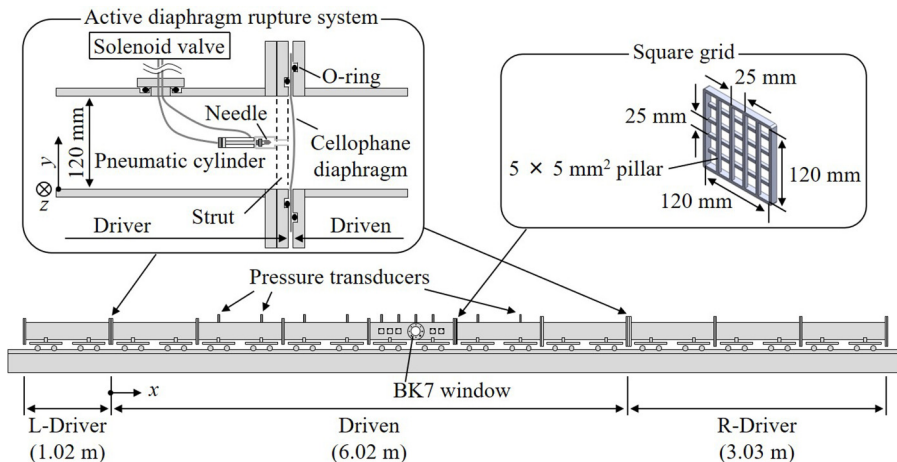


FIG. 1. Schematic illustration of the CD-ST. The active diaphragm rupture system for R-Driver is set symmetrically to that for L-Driver shown in the figure.

have conducted a parametric, experimental investigation of the interaction between a planar shock wave and grid turbulence by varying the representative value of the turbulent Mach number, $\bar{M}_{t,GT}$, and the interaction length, L , which are defined later.

II. APPARATUS

Figure 1 shows the CD-ST used in this study. It has a square cross section of 120 mm \times 120 mm. It is composed of ten 1-m-long segments, and the total length is 10.07 m. The shock tube is subdivided into three sections: the left driver (L-Driver, 1.02 m long), driven section (Driven), and right driver (R-Driver, either 2.03 or 3.03 m long depending on $\bar{M}_{t,GT}$). The driver gas on both sides and the test gas in the low-pressure chamber were room air set at the respective initial pressures. Before the shock tube is operated, L-Driver is separated using one sheet of an 18- μ m-thick diaphragm made of cellophane and R-Driver using one to ten sheets of 36- μ m-thick ones. In order to initiate the shock tube operation, each separation is broken by piercing sheets of the diaphragm with a needle driven by a pneumatic cylinder. The driver air to the cylinder is introduced by opening a solenoid valve (see Fig. 1, SMC Co., SY-3220, nominal opening time 12 ms) with an electrical signal. As shown in the figure, the x axis is defined with its origin at the separation between L-Driver and Driven. The y axis is defined with its origin at the lower inner wall and directs to an upper wall. The z axis has its origin at the front inner wall and directs to the opposite wall. A pair of BK-7 windows with an effective diameter of 110 mm for flow visualization is set in the test section positioned at $x = 3.55$ m. A grid of 5 mm \times 5 mm square pillars with a mesh size of 25 mm is set at $x_{grid} = 4.00$ m. Δx is the distance from the grid toward L-Driver. In order to measure pressure histories, piezoelectric pressure transducers (PCB 113A21, 113B27, or H112A21, rise time 1 μ s) are flush-mounted at the locations indicated in the figure.

III. EXPERIMENTAL CONDITIONS

Figure 2 shows an example of the wave diagram of CD-ST operation. The L-Driver generates the right-running incident shock wave, L-iSW. The right driver (R-Driver) generates the left-running incident shock wave, R-iSW. Behind R-iSW, the post-shock flow is induced. It transitions to grid turbulence beyond the grid at $x = 4.00$ m. After L-iSW and R-iSW collide with each other, the right-running transmitted shock wave, L-tSW, interacts with the grid turbulence in the region [GT]. The distance from the head of the grid turbulence to the shock wave arriving at the center of the

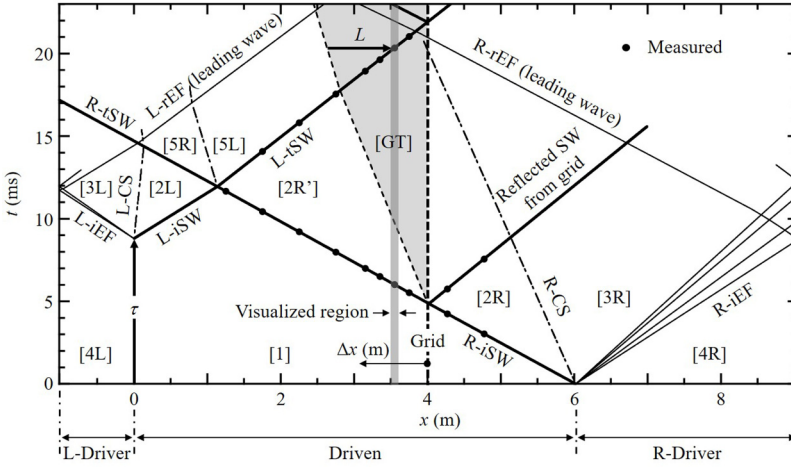


FIG. 2. Example of the space-time (x - t) diagram of shock tube operation: SW, shock wave; EF, expansion fan; CS, contact surface; L-, left; R-, right; i, incident; t, transmitted (except for the region [GT]); r, reflected; $p_{4L} = 55.0$ kPa, $p_1 = 43.0$ kPa, $p_{4R} = 99.9$ kPa, $\tilde{M}_{s,L-iSW} = 1.04$, $\tilde{M}_{t,GT} = 1.1 \times 10^{-2}$, and $L = 981$ mm.

visualized region is defined as the “interaction length” and is designated by L , which is controlled with the difference in the activation timings of the respective pneumatic cylinders, τ .

The operation conditions of CD-ST are tabulated in Table I. Initially, the conditions of L-tSW and the grid turbulence are set according to the “ideal” operation conditions of the two independent drivers [26], which are obtained from Rankine-Hugoniot shock wave relations. The speed of L- and R-iSW were measured by the time-of-flight principle between two pressure transducers as long as they existed in the passage of the respective incident shock waves. Assuming a calorically perfect gas, that is, with a constant value of specific heat ratio, γ , the shock Mach numbers, M_s , of the respective incident shock waves were evaluated by dividing the shock speed by the speed of sound. The incident shock Mach numbers measured experimentally were 1–5 % lower than the

TABLE I. Operation conditions of the counter-driver shock tube and the measured values of shock Mach numbers, M_s , and turbulent Mach number measured at $x = 3.55$ m, $\tilde{M}_{t,GT}$; the initial temperature, 293–298 K; the upper value in M_s , measured via the method of time of flight; the lower value in parentheses in M_s , the ideal value based on Rankine-Hugoniot relations for calorically perfect gas; $\tilde{M}_{s,L-iSW}$, for which the error was evaluated from the run-to-run uncertainty of the time-averaged value seen in Fig. 4; Re_M , mesh Reynolds number; and L_{int} , integral length scale.

p_{4L} (kPa)	p_1 (kPa)	p_{4R} (kPa)	$M_{s,L-iSW}$	$M_{s,R-iSW}$	$\tilde{M}_{s,L-iSW}$	$\tilde{M}_{t,GT}$	Re_M	L_{int} (mm)
55.0	43.0	68.0	1.04 ± 0.01 (1.05)	1.09 ± 0.01 (1.10)	1.047 ± 0.002	0.6×10^{-2}	3.7×10^4	9.7
55.0	43.0	99.9	1.05 ± 0.01 (1.05)	1.17 ± 0.01 (1.19)	1.043 ± 0.002	1.1×10^{-2}	7.7×10^4	24.9
55.0	43.0	310.0	1.04 ± 0.01 (1.05)	1.43 ± 0.01 (1.51)	1.033 ± 0.006	2.4×10^{-2a}	1.9×10^{5a}	

^aEstimated by assuming a linear relation between u and u' .

one-dimensional, laminar analytical solution due to pressure losses mainly caused by the diaphragm rupture devices and the grid.

The shock Mach number of L-tSW, $M_{s,L-tSW}$, was evaluated using the pressure difference across the shock wave:

$$M_{s,L-tSW} = \sqrt{1 + \frac{\gamma + 1}{2\gamma} \frac{\Delta p}{p_*}}, \quad (1)$$

where $p_* = \bar{p}_{2R'}$ or $p_* = \bar{p}_{GT}$ depending on the upstream region (see Fig. 2), and the upper bar represents a time average. As shown in Table I, the shock Mach number at the interface between the regions [2R'] and [GT], $\tilde{M}_{s,L-tSW}$, which was the representative value before interaction with the grid turbulence, was 1.04 ± 0.01 .

As shown in Fig. 2, the gas in the region [GT] experienced a weak shock wave reflection against the grid before passing it. Due to this shock reflection, the temperature in the region [GT] becomes higher than that without the reflection. In this study, using only the R-Driver we measured the distributions of total temperature using a cold wire, and flow velocity using an I-type hot-wire anemometer. In the preliminary experiment, we inserted a cold/hot wire normal to the upper wall of the shock tube at $z = 60$ mm, that is, below the centerline of the upper wall. We noticed that the measurements were influenced by the wire rod itself in the upper half of the shock tube ($60 < y < 120$ mm). Therefore, we employed the measured data only in the lower half of the shock tube. The hot-wire anemometer was calibrated with the total temperature of the grid turbulence, $\bar{T}_{total,GT}$, at $y = z = 60$ mm by setting the corresponding shock Mach number evaluated from Rankine-Hugoniot relations. Varying the initial driven density, ρ_1 , the relation between the mass flux behind the shock wave, $\bar{\rho}_{GT} \bar{u}_{x,GT}$, and the output of the hot-wire anemometer was obtained. The density of the turbulent flow could be written as $\bar{\rho}_{GT} = \bar{p}_{GT}/(R\bar{T}_{GT})$; thus the flow velocity, $\bar{u}_{x,GT}$, was calculated from the signal of the hot-wire anemometer. Assuming isotropic turbulence, from the root-mean-square velocity fluctuation, $u'_{GT} = \sqrt{3}u'_{x,GT}$, and the speed of sound in the grid turbulence, $\bar{a}_{GT} = \sqrt{\gamma R\bar{T}_{GT}}$, the turbulent Mach number was defined as $M_{t,GT} = u'_{GT}/\bar{a}_{GT}$. In the current study, the turbulent Mach number at $x = 3.55$ m, that is, $\Delta x \equiv x_{grid} - x = 0.45$ m on the center axis of the shock tube ($y = z = 60$ mm), is defined as the representative value and denoted as $\tilde{M}_{t,GT}$.

In region [GT], as seen in Fig. 3(a), due to shock reflection against the grid the total temperature in the grid turbulence was increased by 4.5 K. Assuming symmetrical distribution, the total temperature distribution suggested that the grid turbulence had an 80 mm \times 80 mm core on the center axis ($y = z = 60$ mm) with an almost uniform temperature (a variation smaller than 1 K), which was at least 3 K higher than that near the shock tube wall. Figure 3(b) shows an example of hot-wire signal measured on the center axis. Due to the arrival of R-iSW, E suddenly increased due to the shock-induced flow velocity at $T = T_{total,2R'}$. In [GT], due to the increase in the total temperature, E was decreased. The hot-wire anemometer was calibrated only for $T = T_{total,GT} = 340$ K, $y = z = 60$ mm; the calibrated value of u_x is shown also in Fig. 3(b) referring to the right coordinate. Spatial variations of \bar{u}_x and u_x' which were evaluated with the constant temperature of 340 K are shown in Figs. 3(c) and 3(d), respectively. They were obtained only in the grid turbulence zone, which had constant temperature and was not contaminated by expansion waves from R-Driver.

As tabulated in Table I, in the current study three flow conditions, $\tilde{M}_{t,GT} = 0.6 \times 10^{-2}$, 1.1×10^{-2} , and 2.4×10^{-2} , were examined. Note here that only the highest turbulent Mach number, $\tilde{M}_{t,GT} = 2.4 \times 10^{-2}$, was not directly measured because in each run diaphragm fragments damaged the hot wire. Only under this condition $\tilde{M}_{t,GT}$ was estimated for constant turbulent intensity, from an assumption that the velocity fluctuation was proportional to the mean flow velocity evaluated from Rankine-Hugoniot relations. Based on the mesh separation distance of the grid and the averaged flow velocity of the grid turbulence, the mesh Reynolds numbers, Re_M , were evaluated as in Table I. Figure 3(e) shows the variations of the square of the turbulent Mach number on the center axis of the shock tube measured without shock wave interaction. The $M_{t,GT}^2$ decreased with increasing Δx with averaged exponents of -1.7 for $\tilde{M}_{t,GT} = 0.6 \times 10^{-2}$ and -1.3 for $\tilde{M}_{t,GT} = 1.1 \times 10^{-2}$, respectively.

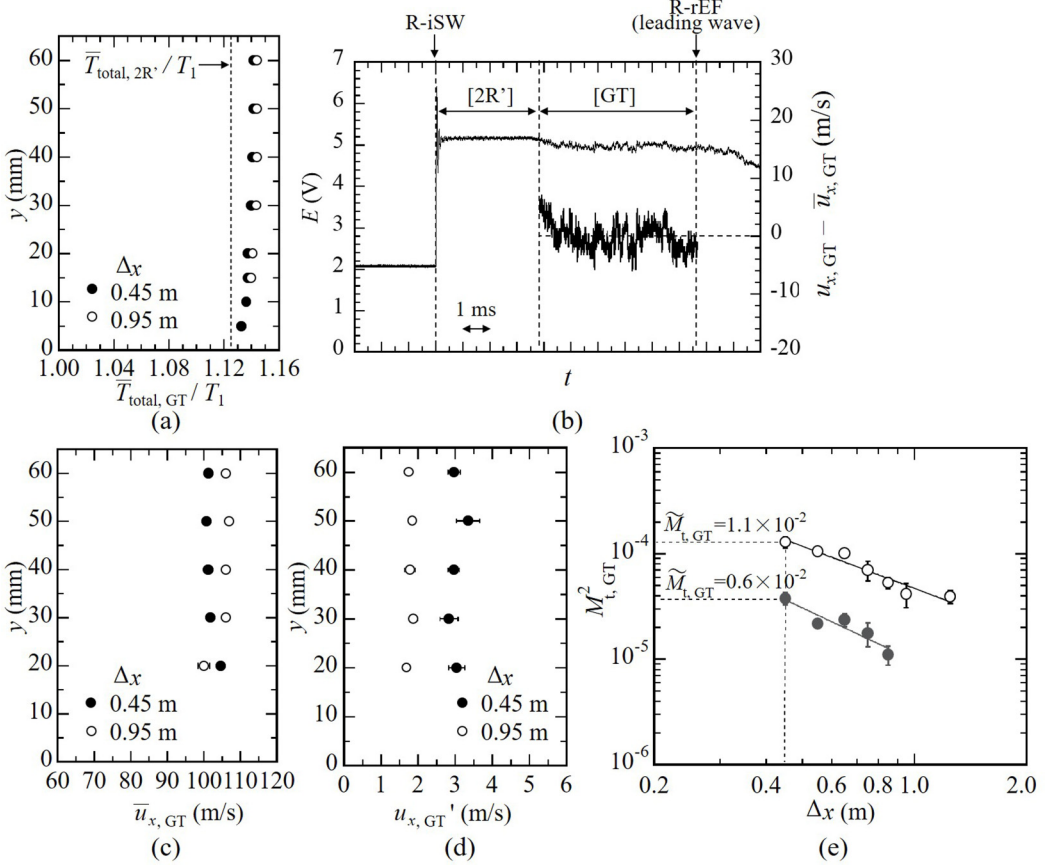
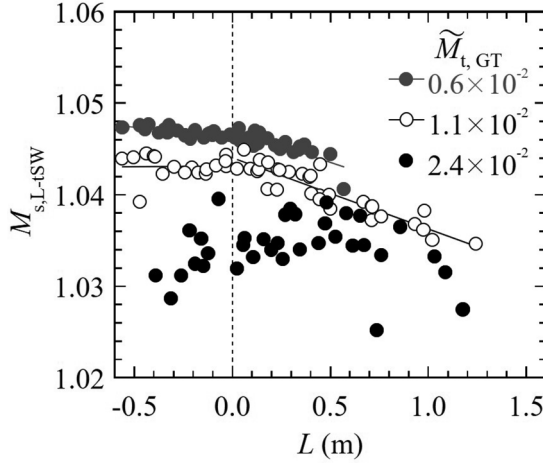


FIG. 3. Characteristics of grid turbulence measured by single driver operations, $z = 60$ mm, $p_1 = 43.0$ kPa: (a) y variation of total temperature of region [GT] measured using a cold wire, $\bar{T}_{\text{total,GT}}$, normalized by T_1 ; (b) example of hot-wire signal, E , and u_x that was obtained based on the calibration with $T = T_{\text{total,2R}}$ at $y = 60$ mm, $\Delta x = 0.45$ m, $y = 60$ mm, and $\bar{u}_x = 102.7$ m/s; (c) y variation of $\bar{u}_{x,\text{GT}}$; (d) y variation of $u_{x,\text{GT}}'$; and (e) Δx variations of $M_{t,\text{GT}}^2$ on the center axis ($y = 60$ mm). The diagram in (a) was obtained using a cold wire; diagrams (b)–(e) were obtained using a hot wire. A small error bar is hidden behind a symbol, (a)–(d) $p_{4R} = 99.9$ kPa, (e) open symbol, $p_{4R} = 99.9$ kPa; solid symbol, $p_{4R} = 68.0$ kPa.

In the case of $\tilde{M}_{t,\text{GT}} = 1.1 \times 10^{-2}$, the turbulent Mach number \tilde{M} decreased down to 0.6×10^{-2} (by 45%) from $\Delta x = 0.45$ m to 1.25 m. This tendency was consistent with the results of previous studies using low-speed wind tunnels [27,28] and a study using a shock tube [29]. Therefore, in the present study, we see the interaction processes between a shock-tube-driven shock wave and the decaying grid turbulence.

IV. RESULTS AND DISCUSSIONS

Figure 4 shows the variations of the shock Mach number of L-tSW evaluated using Eq. (1) as a function of L . In the cases of $\tilde{M}_{t,\text{GT}} = 0.6 \times 10^{-2}$, the experimental data best fit to a linear variation with $d\tilde{M}_{s,\text{L-tSW}}/dL = -2.1 \times 10^{-3} \text{ m}^{-1}$ in $L < 0$ and $= -7.0 \times 10^{-3} \text{ m}^{-1}$ in $L > 0$, respectively. With $\tilde{M}_{t,\text{GT}} = 1.1 \times 10^{-2}$, $d\tilde{M}_{s,\text{L-tSW}}/dL = -0.1 \times 10^{-3} \text{ m}^{-1}$ in $L < 0$ and $= -7.7 \times 10^{-3} \text{ m}^{-1}$ in $L > 0$, respectively. In both cases, a higher Mach number decrease rate was obtained in $L > 0$, although the influence of $\tilde{M}_{t,\text{GT}}$ on the decrease rate is not necessarily clear. In the case of $\tilde{M}_{t,\text{GT}} = 2.4 \times 10^{-2}$ the data scatter is too large to characterize the M_s variation.

FIG. 4. $M_{s,L-SW}$ vs L .

Flow visualization was performed with a side-view shadowgraph set up through a pair of BK-7 windows with a long, collimated beam path of 12 m after the test section. A high-speed camera (Phantom v1211, Vision Research Inc.; 256 pixels \times 256 pixels, 100 kfps) and a synchronized pulsed diode laser (CAVILUX smart, Cavitar Ltd.; wavelength 640 nm) were used for the visualization. The quality of the point light source was improved by using a sheet of holographic diffuser (Edmund Optics Inc., diverging angle 60°). To eliminate unnecessary background noise, the rough gray-scale image was digitally subtracted by a reference image obtained under the initial, quiescent condition before a flow event of the present interest was initiated.

Figure 5 shows the side-view shadowgraph images of shock wave–turbulence interaction with various values of $\tilde{M}_{t,GT}$ and L . Each line corresponds to a constant $\tilde{M}_{t,GT}$; the leftmost image corresponds to an image before interaction ($L < 0$), then increasing L to the right. For a two-dimensional flow observed with the present side-view shadowgraph system, in principle, the gray scale of a visualized image should scale with the second derivative of density; across a shock wave from left to right, the gray scale should vary from a baseline to bright and dark, and finally back to the baseline. Physically, this density variation across the side view of a perfectly planar shock wave should occur within several mean free paths, which, in the present case, is of the order of 0.1 μm . However, the visualized density variation has a thickness of approximately 1 mm, which limits the practical, spatial resolution of the shape and location of the shock wave. The effective exposure duration of a frame was determined by the pulsed diode laser duration of 20 ns, during which the shock moves only by 7 μm . This blur is two orders of magnitude smaller than the spatial resolution of the shadowgraph image.

For each value of $\tilde{M}_{t,GT}$, the side view of the shock wave before the interaction is shaped as an almost straight line within the above-mentioned spatial resolution. However, in each case, the shape of the shock wave becomes slightly convex toward the propagation direction, i.e., to the right. This is due to the flow velocity and static temperature distribution over the boundary layer in the post-shock flow in the region [GT] (Fig. 2). Before the interaction, each shock wave does not have significant higher-order fluctuations. However, in each case, propagating through the grid turbulence, the shock wave profile starts to experience higher-order deformations and the thickness of the side-view shock wave zone increases with the increase in L . As expected from the results of numerical simulations published so far [18–24], the shock wave front should experience local deformation owing to velocity fluctuation in the turbulence. In the present study, the shape of the shock wave is observed only from the side-view shadowgraph; hence, the shadowgraph image should be the projection covering the shock wave front. When passing through a deformed shock

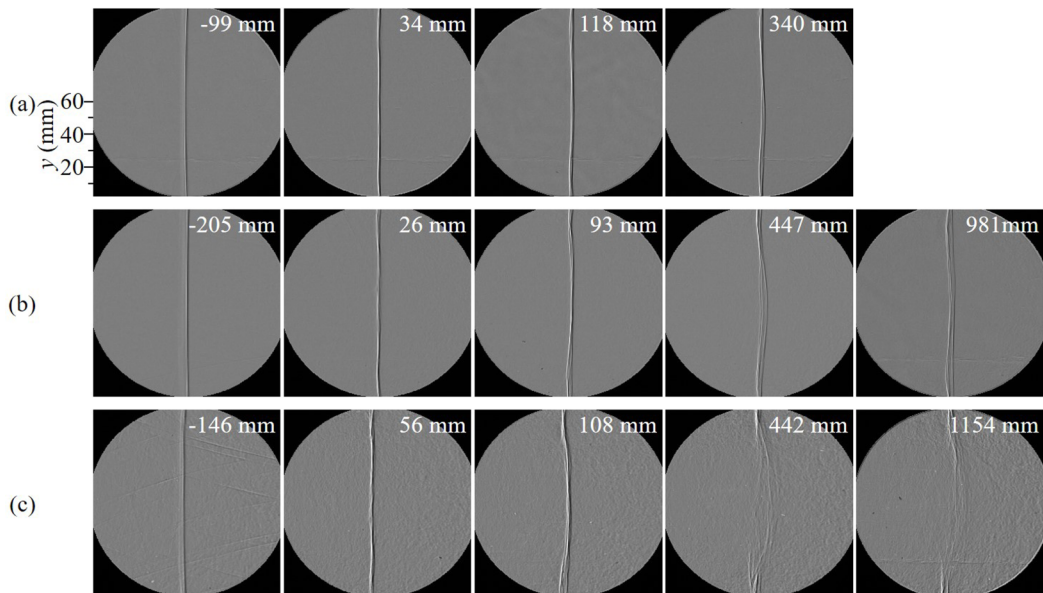


FIG. 5. Shadowgraph images of a shock wave propagating through turbulence with various values of L indicated as a white number in each frame. A negative value corresponds to the image before interaction. (a) $\tilde{M}_{t,GT} = 0.6 \times 10^{-2}$, (b) $\tilde{M}_{t,GT} = 1.1 \times 10^{-2}$, and (c) $\tilde{M}_{t,GT} = 2.4 \times 10^{-2}$.

wave front, the thickness of the corresponding zone should be increased. This interpretation is applicable to all $\tilde{M}_{t,GT} = 0.6 \times 10^{-2}$ and $\tilde{M}_{t,GT} = 1.1 \times 10^{-2}$ images.

The same interpretation also applies to the case of $\tilde{M}_{t,GT} = 2.4 \times 10^{-2}$ up to $L = 108$ mm. However, in the images for $L = 442$ and 1154 mm, the shock wave profile is not continuous but becomes dispersed into several broken curves. At some vertical locations, the shock profile is not well recognized. In the present study, as we only visualized the side-view shadowgraph, a three-dimensional shock wave front profile cannot be obtained. However, it has been demonstrated that, within the present sensitivity to density variation, the shock wave front has a profile consistent with a “broken” profile. That is, the shock wave profile is fragmented into several discontinuous ones.

Donzis [20] and Larsson *et al.* [24] concluded from the results of the theoretical analysis and their numerical simulation that, if the following critical condition is satisfied, locally, the relative flow speed across the wave front can become subsonic so that the shock wave front becomes “broken” at such locations:

$$M_t \geq 0.6(M_s - 1). \quad (2)$$

As seen in Fig. 6, only in the case of the highest turbulent Mach number is the above critical condition barely satisfied, which is thus consistent with the numerical prediction. However, the shock wave morphology observed in the turbulence strongly depends on the interaction length, L . The present experimental study has confirmed the importance of this parameter, thereby warranting further investigations to generalize the shock wave–turbulence interaction with respect to the interaction length.

V. CONCLUSION

From the current study in which the impacts of the grid turbulence interaction in the $\tilde{M}_{t,GT}$ range of 0.6×10^{-2} to 2.4×10^{-2} on a planar shock wave with $\tilde{M}_{s,L-tSW} \simeq 1.03 - 1.04$ was experimentally investigated using the counter-driver shock tube, the following conclusions have

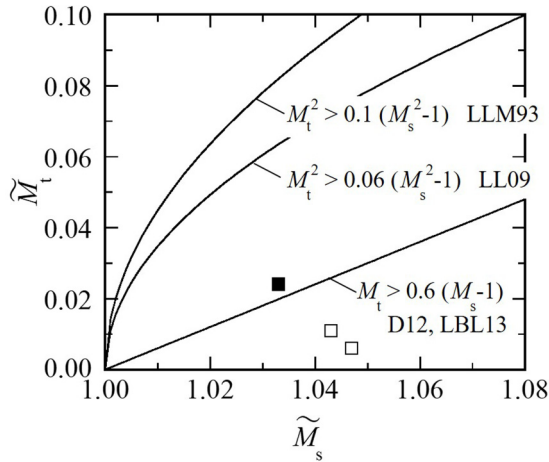


FIG. 6. Broken shock criteria and the shock front condition in the experiment on \tilde{M}_s - \tilde{M}_t coordinates; solid symbols, broken shock front profile with the largest L ; open symbols, continuous shock front profile; LLM93, Ref. [17]; LL09, Ref. [18]; D12, Ref. [20]; and LBL13, Ref. [24].

been obtained: Within the resolvable experimental data of $\tilde{M}_{t,GT} = 0.6 \times 10^{-2}$ and 1.1×10^{-2} , M_s became a decreasing function of L . The thickness of the shock front side-view profile increased as $\tilde{M}_{t,GT}$ and L increased. With $\tilde{M}_{t,GT} = 2.4 \times 10^{-2}$ and $L > 200$ mm, the shock front profile became fragmented. The condition for the fragmentation is consistent with the proposed broken shock criterion predicted by the numerical studies of Donzis [20] and Larsson *et al.* [24].

ACKNOWLEDGMENTS

The authors gratefully acknowledge the technical information about shock tube design received from T. Abe, Institute of Space and Astronautical Science, Japan Aerospace Exploration Agency, and K. Suzuki, University of Tokyo, and the kind donation of cellophane diaphragm by Futamura Chemical Co., Ltd. We are also grateful for the valuable comments and advice from K. Nagata, Nagoya University, and the valuable technical assistance of N. Shiraki, M. Nakakimura, and A. Saito, Technical Division, Nagoya University. This research was supported by the JSPS KAKENHI Grants No. 15H02321, No. 18H03813, and No. 17J10997.

-
- [1] H. H. Hubbard, D. J. Maglieri, V. Huckel, and D. A. Hilton, Ground measurements of sonic-boom pressures for the altitude range of 10,000 to 75,000 feet, NASA Report No. TR R-198, 1964.
 - [2] E. J. Kane, Some effects of the atmosphere on sonic boom, NASA Report No. SP-147, 49, 1967.
 - [3] H. S. Ribner, P. J. Morris, and W. H. Chu, Laboratory simulation of development of superbooms by atmospheric turbulence, *J. Acoust. Soc. Am.* **53**, 926 (1973).
 - [4] B. Lipkens and D. T. Blackstock, Model experiment to study sonic boom propagation through turbulence, *J. Acoust. Soc. Am.* **103**, 148 (1998).
 - [5] J.-H. Kim, A. Sasoh, and A. Matsuda, Modulations of a weak shock wave through a turbulent slit jet, *Shock Waves* **20**, 339 (2010).
 - [6] T. Tamba, D. Furukawa, Y. Aoki, M. Kayumi, A. Iwakawa, A. Sasoh, T. Matsunaga, M. Izumo, Y. Sugiyama, T. Matsumura, and Y. Nakayama, Field experiment of blast wave pressure modulation past a turbulent flow, *Sci. Tech. Energetic Materials* **77**, 91 (2016).
 - [7] A. Sasoh, T. Harasaki, T. Kitamura, D. Takagi, S. Ito, A. Matsuda, K. Nagata, and Y. Sakai, Statistical behavior of post-shock overpressure past grid turbulence, *Shock Waves* **24**, 489 (2014).

- [8] T. Kitamura, K. Nagata, Y. Sakai, A. Sasoh, and Y. Ito, Changes in divergence-free grid turbulence interacting with a weak spherical shock wave, *Phys. Fluids* **29**, 065114 (2017).
- [9] K. Inokuma, T. Watanabe, K. Nagata, A. Sasoh, and Y. Sakai, Finite response time of shock wave modulation by turbulence, *Phys. Fluids* **29**, 051701 (2017).
- [10] S. Barre, D. Alem, and J. P. Bonnet, Experimental study of a normal shock/homogeneous turbulence interaction, *AIAA J.* **34**, 968 (1996).
- [11] S. Barre, D. Alem, and J. P. Bonnet, Reply by the authors to H. S. Ribner, *AIAA J.* **36**, 495 (1998).
- [12] D. S. Dosanjh, Interaction of grids with traveling shock waves, NACA Report No. TN-3680, 1956.
- [13] A. Honkan and J. Andreopoulos, Rapid compression of grid-generated turbulence by a moving shock wave, *Phys. Fluids A Fluid Dyn.* **4**, 2562 (1992).
- [14] A. Honkan, C. B. Watkins, and J. Andreopoulos, Experimental study of interactions of shock wave with free-stream turbulence, *J. Fluid Eng.* **116**, 763 (1994).
- [15] S. Xanthos, G. Briassulis, and Y. Andreopoulos, Interaction of decaying freestream turbulence with a moving shock wave: Pressure field, *J. Propul. Power* **18**, 1289 (2002).
- [16] J. H. Agui, G. Briassulis, and Y. Andreopoulos, Studies of interactions of a propagating shock wave with a decaying grid turbulence: Velocity and vorticity fields, *J. Fluid Mech.* **524**, 143 (2005).
- [17] S. Lee, S. K. Lele, and P. Moin, Direct numerical simulation of isotropic turbulence interacting with a weak shock wave, *J. Fluid Mech.* **251**, 533 (1993).
- [18] J. Larsson and S. K. Lele, Direct numerical simulation of canonical shock/turbulence interaction, *Phys. Fluids* **21**, 126101 (2009).
- [19] D. A. Donzis, Amplification factors in shock-turbulence interactions: Effect of shock thickness, *Phys. Fluids* **24**, 011705 (2012).
- [20] D. A. Donzis, Shock structure in shock-turbulence interactions, *Phys. Fluids* **24**, 126101 (2012).
- [21] Y. Tian, F. A. Jaber, Z. Li, and D. Livescu, Numerical study of variable density turbulence interaction with a normal shock wave, *J. Fluid Mech.* **829**, 551 (2017).
- [22] L. Ryu and D. Livescu, Turbulence structure behind the shock in canonical shock–vortical turbulence interaction, *J. Fluid Mech.* **756**, R1 (2014).
- [23] D. Livescu and L. Ryu, Vorticity dynamics after the shock–turbulence interaction, *Shock Waves* **26**, 241 (2016).
- [24] J. Larsson, I. Bermejo-Moreno, and S. K. Lele, Reynolds- and Mach-number effects in canonical shock-turbulence interaction, *J. Fluid Mech.* **717**, 293 (2013).
- [25] S. K. Lele, Shock-jump relations in a turbulent flow, *Phys. Fluids* **4**, 2900 (1992).
- [26] T. Tamba, T. M. Nguyen, K. Takeya, T. Harasaki, A. Iwakawa, and A. Sasoh, Counter-driver shock tube, *Shock Waves* **25**, 667 (2015).
- [27] P. E. Roach, The generation of nearly isotropic turbulence by means of grids, *Int. J. Heat Fluid Flow* **8**, 82 (1987).
- [28] T. Kitamura, K. Nagata, Y. Sakai, A. Sasoh, O. Terashima, H. Saito, and T. Harasaki, On invariants in grid turbulence at moderate Reynolds numbers, *J. Fluid Mech.* **738**, 378 (2014).
- [29] G. Briassulis, J. H. Agui, and Y. Andreopoulos, The structure of weakly compressible grid-turbulence, *J. Fluid Mech.* **432**, 219 (2001).